Self-Assembled Virus-like Particles with Magnetic Cores

Xinlei Huang,[†] Lyudmila M. Bronstein,*,[†] John Retrum,[†] Chris Dufort,[†]
Irina Tsvetkova,[‡] Stella Aniagyei,[†] Barry Stein,[§] Galen Stucky,[∥]
Brandon McKenna,[∥] Nicholas Remmes,[⊥] David Baxter,[⊥] C. Cheng Kao,[#] and
Bogdan Dragnea*,[†]

*Department of Chemistry, Indiana University, 800 East Kirkwood Avenue,
Bloomington, Indiana 47405, Nesmeyanov Institute of Organoelement Compounds,
28 Vavilov Street, Moscow 119991, Russia, Department of Biology,
Indiana University, 1001 East Third Street, Bloomington, Indiana 47405,
Department of Chemistry and Biochemistry, University of California at Santa Barbara,
Department of Physics, Indiana University, 727 East Third St.,
Bloomington, Indiana 47405, and Department of Biochemistry & Biophysics,
Texas A&M University, College Station, Texas 77843*

ABSTRACT

Efficient encapsulation of functionalized spherical nanoparticles by viral protein cages was found to occur even if the nanoparticle is larger than the inner cavity of the native capsid. This result raises the intriguing possibility of reprogramming the self-assembly of viral structural proteins. The iron oxide nanotemplates used in this work are superparamagnetic, with a blocking temperature of about 250 K, making these virus-like particles interesting for applications such as magnetic resonance imaging and biomagnetic materials. Another novel feature of the virus-like particle assembly described in this work is the use of an anionic lipid micelle coat instead of a molecular layer covalently bound to the inorganic nanotemplate. Differences between the two functionalization strategies are discussed.

A. Introduction. Magnetic nanoparticles (NPs) have received considerable attention due to the promise they bring in a wide variety of biomedical applications such as contrast enhancement agents for magnetic resonance imaging (MRI),[1,2] bioprobes,[3] cell sorters,[4,5] etc. Usually, superparamagnetic NPs having reversible magnetization are preferred to ferromagnetic ones that have permanent magnetization because they are less prone to aggregation.

When magnetic NPs are used as bioprobes, proper functionalization is required for biocompatibility and to create an array of external functionalization sites. Both goals can be achieved when the nanoparticle is actually encapsulated in a viral capsid.[6-10]

In this paper, we explore the templated self-assembly of brome mosaic virus (BMV) capsids around negatively charged iron oxide NPs leading to hybrid magnetic virus-like particles (VLPs). Due to the high relaxivity of iron oxide particles,[11,12] the innate biocompatibility of virus capsids, and the possibility of further engineering of capsid surface sites, superparamagnetic VLPs are potentially suitable as specific MRI contrast agents for plant studies, especially in relation with systemic virus movement and for better understanding of the interaction between plant systems used in the production of biopharmaceuticals with recombinant viruses.[13-15]

BMV is an icosahedral virus with a $T = 3$ lattice.[16] It is composed of 180 identical proteins, which form pentameric or hexameric subunits and a multipartite genome containing four single-strand RNA molecules. The capsid of the wild-type BMV has an outside diameter of 28 nm while the inner core diameter is around 18 nm.[16] BMV virion assembly appears to be driven by initial interactions between the very positively charged amino-termini of the coat protein and the negatively charged RNA, followed by weaker protein–protein interactions in between.[17] The protein–nucleic acid interaction appears to be mostly nonspecific.[18]

Virus-based nanomaterial platforms have used the interior surface of the virus capsid for directed synthesis of both organic and inorganic NPs. For example, the native positively charged inner capsid of the icosahedral cowpea chlorotic

* To whom correspondence should be addressed. E-mail: lybronst@indiana.edu; dragnea@indiana.edu.
† Department of Chemistry, Indiana University.
‡ Nesmeyanov Institute of Organoelement Compounds.
§ Department of Biology, Indiana University.
∥ Department of Chemistry and Biochemistry, University of California at Santa Barbara.
⊥ Department of Physics, Indiana University.
Department of Biochemistry & Biophysics, Texas A&M University.

mottle virus (CCMV) was used to synthesize spatially constrained nanoparticles of polyoxometalate salts (tungstates $H_2W_{12}O_{42}^{10-}$ and vanadates $V_{10}O_{28}^{6-}$).[19] In addition, the inner surface of the CCMV capsid could be changed from positively to negatively charged, which directed the surface nucleation of Fe_2O_3, Fe_3O_4, or Co_2O_3.[20]

An alternative way to utilize the architecture of the virus capsid is to encapsulate by self-assembly surface-modified nanoparticles. The nanoparticle cores replace the native nucleic acids and participate to recruit and organize the capsid proteins during the self-assembly process. An advantage of this approach is the possibility to form NPs synthesized through high-temperature organometallic chemistry[21−23] that can overcome challenges associated with NP synthesis and protein stability.

Formation of BMV VLPs has been previously reported for negatively charged gold nanoparticles with diameters ranging between 6 and 12 nm[24,25] and quantum dots with a diameter of ∼4 nm.[26] Here we report on the encapsulation of phospholipid-protected superparamagnetic nanoparticle cores. This approach expands the types of payload that can be carried by a virus cage. In particular, insoluble proteins could be transported to their targets. Variations in the encapsulation efficiencies have been found, which can be explained through interplay between the surface charge density and lipid packing on the core surface.

B. Experimental Part. B.1. Materials. $FeCl_3\cdot6H_2O$ (98%), docosane (99%), eicosane (99%), and octadecane (99%) were from Sigma-Aldrich and used as received. Hexanes (85%), ethanol (95%), and acetone (99.78%) were from EMD and used as received. Chloroform (Mallinckrodt, 100%), oleic acid (TCI, 95%), and oleic acid sodium salt (ScienceLab.com, 95%) were used without purification. 1,2-Distearoyl-*sn*-glycero-3-phosphoethanolamine-*N*-[carboxy-(polyethylene glycol)2000] (ammonium salt) (HOOC-PEG-PL, 2000 Da PEG [PEG is poly(ethylene oxide)], Avanti, 99%) was used as received. Capsid proteins were obtained from BMV extracted from *Agrobacterium* infiltrated *N. benthamiana* plants.[27]

B.2. Syntheses. B.2.1. Synthesis of Iron Oxide Nanoparticles. Spherical iron oxide nanoparticles with mean diameters of 20.1, 10.6, and 8.5 nm were synthesized using thermal decomposition of iron oleate by modification of a published procedure.[22,28] In a typical experiment for 20.1 nm NPs, 2.78 g (3 mmol) of iron oleate complex (thermally treated at 70 °C in a vacuum oven for 24 h),[28] 0.96 mL of oleic acid (3 mmol), and 10 mL of docosane (hydrocarbon $C_{22}H_{46}$, solid at room temperature) were mixed in a three-neck round-bottom reaction flask. The mixture was first heated to 60 °C to melt the solvent, and the reactants were dissolved under vigorous stirring. Then the temperature was increased to 370 °C with a heating rate of 3.3 °C/min (using a digital temperature controller) under stirring and refluxing for 3 min. During this operation, the initial reddish-brown color of the reaction solution turned brownish-black. The resultant solution was then cooled down to 50 °C, and a mixture of 10 mL of hexane and 40 mL of acetone was added into the reaction flask to precipitate the NPs. The NPs were

separated by centrifugation and washed three times by the hexane and acetone mixture. After being washed, the resultant NPs were again centrifuged and dissolved in chloroform for long-term storage.

Alternatively, only a small fraction of the reaction solution was precipitated as described above, while the major fraction was kept as a solid and precipitated when needed. The latter procedure allows one to avoid NP aggregation in a liquid solution at prolonged storage times. Spherical nanoparticles of 8.5 and 10.6 nm in diameter were prepared in octadecane for 30 and 60 min, respectively, using Fe oleate dried at 30 °C in a vacuum oven for 24 h.[28]

B.2.3. Functionalization of Iron Oxide Nanoparticles with HOOC-PEG-PL. HOOC-PEG-PL micelles encapsulating iron oxide nanoparticles were formed by adopting the procedure described for quantum dots.[29] In a typical experiment, 1.7 mg of oleic acid coated NPs of 20.1 nm were dissolved in 1 mL of chloroform. HOOC-PEG-PL (1.4 mg) was added to the solution and completely solubilized by sonication for 5 min followed by the removal of chloroform by evaporation. The residual solid was heated in an 80 °C bath for 5 min, and 1 mL of deionized water was added immediately. After 5 min of vigorous stirring, a uniform transparent brownish-black aqueous solution was formed. Ultracentrifugation (90000g, 2 h, three times) was applied to remove unbound COOH-PEG-PL.

B.2.4. VLP formation by virus capsid self-assembly around magnetic NPs. BMV capsids are most stable at low to moderate ionic strength buffers and at a pH 5.0, but it experiences a profound structural transition when the pH is increased from 5 to 7. To assemble VLPs with iron oxide nanoparticles, some modifications were made to published protocols[30,31] due to the lower stability of the HOOC-PEG-PL coated NPs in high ionic strength solutions. A typical procedure to encapsulate iron oxide NP is described in the Supporting Information.

B.3. Characterization of NPs. Dynamic light scattering (DLS) measurements were carried out with a Zetasizer NanoS (Malvern Instruments). Samples for DLS were first diluted, then sonicated for 10−20 min, and filtered with a 0.2 μm syringe filter. Measurement duration was set to be determined automatically, and data were averaged from at least three runs. Intensity and volume distributions of the particle sizes were recorded.

The UV−vis absorption intensity of a series of standard chloroform solutions of iron oxide nanoparticles with predetermined concentrations was measured at $\lambda = 300$ nm using the Cary 100 Bio instrument (Varian) to plot a calibration curve of intensity versus concentration. The extinction coefficient calculated from the calibration curve was 14.25 $(g/L)^{-1}$ $(cm)^{-1}$ (Figure S1 in Supporting Information). Concentrations of the target solution were determined by its absorption at the same wavelength, and weight concentration was derived using the Lambert−Beer law. To calculate the number concentration, the weight of a single NP was calculated based on its diameter (from transmission electron microscopy size analysis) and density for FeO (5.7 g/cm^3).

Concentrations of BMV proteins were determined by UV–vis absorption using a NanoDrop ND-1000 UV–vis spectrophotometer. Absorbance at 280 nm was used to find the concentration of proteins using Lambert–Beer's law. The extinction coefficient of the protein was taken as 0.82 $(g/L)^{-1} (cm)^{-1}$.

Electron-transparent NP specimens for transmission electron microscopy (TEM) were prepared by placing a drop of dilute solution onto a carbon-coated Cu grid. Images were acquired at an accelerating voltage of 80 kV on a JEOL JEM1010 transmission electron microscope and analyzed with the Adobe Photoshop software package and the Scion Image Processing Toolkit to estimate NP diameters. Between 150 and 300 NPs were used for analysis. Electron energy-loss spectroscopy (EELS) for elemental mapping was carried out with a JEOL 2200FS.

VLP preparation for TEM used 10 μL of the capsid solution on a carbon-coated copper grid. After 10 min, the excess solution on the grid was removed with filter paper. Ten microliters of saturated uranyl acetate was used to stain the viruses for 10 min. Excess solution was removed by blotting with filter paper. The sample was then left to dry for several minutes.

Standard Fourier transform infrared (FTIR) spectra were recorded on a Nicolet spectrometer by placing the sample on a KBr disk and evaporating the chloroform or THF. Attenuated total reflectance (ATR) FTIR spectroscopy of functionalized magnetic NPs was recorded with a Nicolet Magna-IR 550 spectrometer. Standard solutions with different concentrations of COOH-PEG-PL were placed on a silicon crystal prism, evaporated, and examined by ATR-FTIR. A linear calibration curve of the intensity of a band characteristic of carbonyl groups (around 1740 cm^{-1}) versus concentration of the lipid solution was plotted (Figure S2, Supporting Information). The amount of the HOOC-PEG-PL molecules on the nanoparticle surface was determined for each sample using ATR-FTIR spectroscopy. The intensity of the carbonyl band was compared with the calibration curve to derive the weight concentration of the ligands on the NPs. Ligand density on each particle was calculated by dividing the number concentration of ligands by a number concentration of particles (measured and calculated by UV–vis spectroscopy).

Zeta-potential measurements were performed using a Malvern Zetasizer Nano ZS equipped with an MPT-2 autotitrator containing 0.25 M HCl and 0.25 M NaOH. Nanoparticle solutions were diluted with 0.10 M KNO_3 to minimize ionic strength effects from the acid and base. The software was programmed to titrate the solutions from the starting pH down to pH 3, in increments suited to each solution buffer capacity. Zeta potential and pH values were measured before and after sample recirculation through the folded capillary cell. Data were processed using the absorption of bulk iron oxide, the indices of refraction of iron oxide and solvent, and the viscosity of the pure water. The Smoluchowski approximation was used to convert the electrophoretic mobility to a zeta potential.
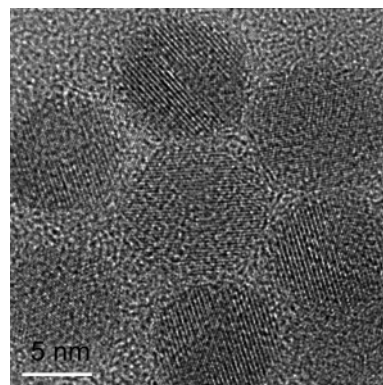

Figure 1. HRTEM of the 8.5 nm iron oxide NPs.

Magnetic measurements were carried out using a Quantum Design MPMS XL magnetometer. Zero-field cooling curves were taken by cooling the sample in null field (± 0.1 Oe) down to 4.5 K, applying a 50 Oe field, and then measuring the magnetization in regular temperature increments up to 300 K. For the FC curves, the samples were cooled in the 50 Oe field to 4.5 K and magnetization measurements were repeated in regular temperature increments up to 300 K.

Magnetic force microscopy (MFM) was performed using an Asylum Research (Santa Barbara, CA) MFP3D atomic force microscope. Noncontact imaging and magnetic measurements were done with standard MFM cantilevers coated with 50 nm of CoCr and magnetized prior to use. Samples were prepared by applying a diluted drop of NPs suspended in chloroform or VLPs suspended in water onto a freshly cleaved sheet of mica which was then rinsed with pure solvent and allowed to dry. All magnetic measurements were done at a constant lift height of 50 nm to decouple the tip from short-range interactions with the surface. This was done by first mapping the topography of the sample and then adding an offset to the MFM trace to ensure constant sample–tip distance despite variations in the surface morphology.

C. Results and Discussion. C.1. Magnetic Cores. To develop magnetic NPs which can be encapsulated by BMV capsids, we modified a previously published procedure[22] to yield iron oxide nanoparticles of tunable size using thermal decomposition of iron oleate. Monodisperse spherical nanoparticles of 20.1 nm ± 4.1%, 10.6 nm ± 7.7%, and 8.5 nm ± 5.2% in diameter have been prepared (Figure S3 in Supporting Information).[28] The XRD data show that iron oxide nanoparticles contain both wüstite ($Fe_{(1-x)}O$) and spinel (most likely Fe_3O_4). The fraction of spinel depends on the conditions of the nanoparticle formation.[28] A high-resolution TEM (HRTEM) picture of the 8.5 nm NPs is presented in Figure 1.

C.2. Functionalization of Nanoparticles with PEGylated Phospholipids. As-prepared magnetic nanoparticles are hydrophobic. PEGylated phospholipids have been already successfully explored for imparting water solubility and in some cases functionality to hydrophobic particles in biological applications.[29,32–34] Here carboxy-terminated PEGylated phospholipids (HOOC-PEG-PL) mixed with the as-prepared particles yield micelle-coated nanoparticles. The assembly
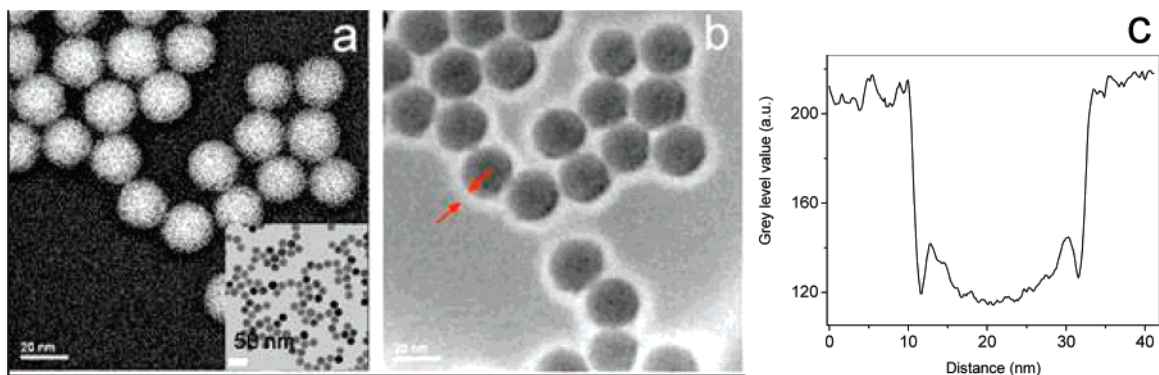
Figure 2. Iron (a) and carbon (b) compositional EELS maps of 20.1 nm NPs coated with HOOC-PEG-PL presented in inset to (a). Red arrows indicate the HOOC-PEG-PL shell. (c) Average gray level cross section through negatively stained, lipid-coated nanoparticles shown in Figure S4, Supporting Information.
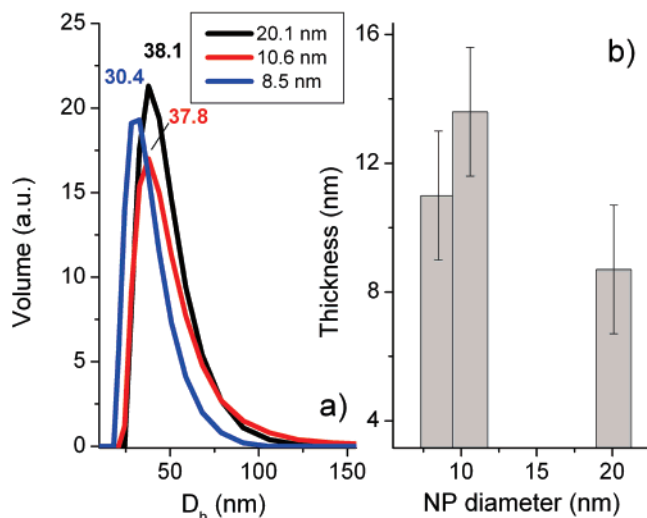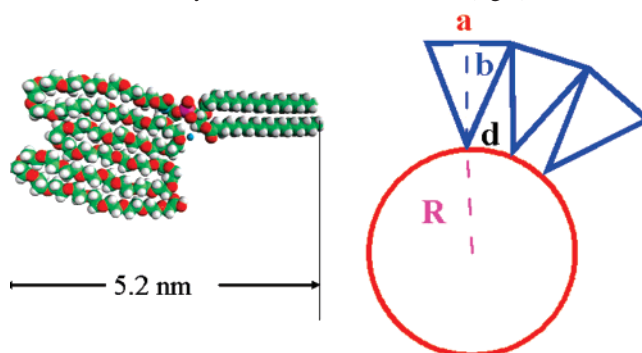

Figure 3. (a) DLS volume distributions vs hydrodynamic diameter for 20.1, 10.6, and 8.5 nm nominal diameter NPs coated with HOOC-PEG-PL. Numbers on the graph indicate D_h (nm) at the peak. (b) Hydrodynamic diameters were used to estimate variations in the thickness of the micelle wall as a function of the particle diameter.

Scheme 1. The Structure of HOOC-PEG-PL in a Crystal Phase (left)[35] and a Cartoon Showing Calculation of the Lipid Density on the of the NP Surface (right)

process is driven by hydrophobic interactions between the lipids and the oleic acid tails on the nanoparticle surface. The surface of the micelle surrounding the nanoparticle is thus characterized by an anionic surface charge (from the terminal −COOH groups) and hydrophilic properties (from the PEG chains), two important characteristics for encapsulation.[25]

Figure 2 shows the TEM image of the 20.1 nm NPs coated with PEGylated phospholipids (inset), their elemental composition obtained from EELS mapping and estimation of the shell thickness obtained from the stained image presented in Figure S4 (see Supporting Information). From the inset, one can see that the particles are well dispersed in water, with no apparent aggregates. However, the HOOC-PEG-PL shell is difficult to see. Averaging similarly sized particles on stained micrographs (Figure S4, Supporting Information) and taking a cross section through a diameter shows a narrow dark ring ~1.8 nm thick, which is probably the stained and dried lipid (Figure 2c). The fact that the stain penetrates the lipid and is then concentrated by drying supports the view

that the uranyl cations have free access through a rather diffuse layer. This is different from thiolated HOOC-PEG on gold NPs, which appeared impermeable to the stain and appear as a brighter surface layer than the background.[25]

Chemical mapping by spatially resolved EELS on unstained samples is presented in panels a and b of Figure 2. The iron and carbon compositional maps reveal that the carbon-rich layer of HOOC-PEG-PL extends to ~4.0 nm (red arrows in Figure 2b). The diffuse layer view, suggested by negative staining results, is also supported by the fact that the particles can still come close to the point of touching despite the estimated thickness of 4 nm (Figure 2).

Together, the stained and the EELS electron micrographs set the thickness of the lipid layer between 1.8 and 4.0 nm.

To evaluate the lipid shell thickness at conditions relevant to VLP assembly, solution properties had to be studied. It is noteworthy that phospholipid coated NPs form stable aqueous solutions: no precipitation was observed for months.

Volume distributions of hydrodynamic diameters (D_h) of NPs coated with HOOC-PEG-PL are presented in Figure 3. The D_h values at peak positions and the TEM-measured NP diameters allowed estimates for the lipid layer thicknesses as a function of NP radius. They are ~9.0 ± 0.1 nm for 20.1 nm coated NPs, ~14.0 ± 0.3 nm for 10.6 nm coated NPs, and ~11.0 ± 0.05 nm for 8.5 nm coated NPs. This result indicates that the micelle wall thickness may vary significantly (~50%) between 8.5 and 20.1 nm NP diameters.

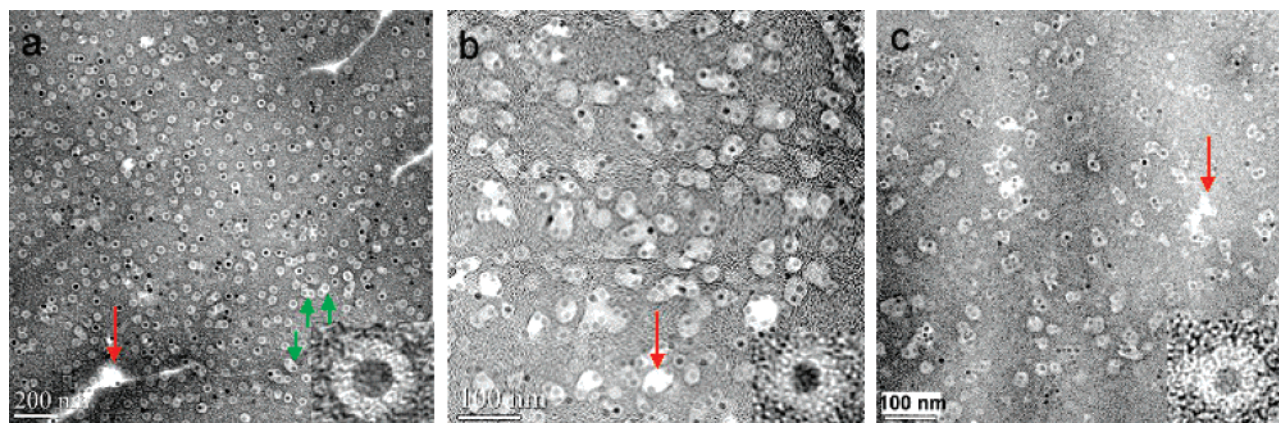**Figure 4.** TEM images of VLPs formed by self-assembling of BMV proteins around 20.1 (a), 10.6 (b), and 8.5 (c) nm spherical NPs coated with HOOC-PEG-PL. In all images dark circular spots are NPs. Light colored areas around NPs are BMV shells. The HOOC-PEG-PL shells are not visible. Irregular white spots indicated by red arrows are defects in staining. The green arrows in (a) indicate merged (peanut shaped) VLPs. Lower insets show individual VLPs at a higher magnification.

Note that the fully extended length of HOOC-PEG-PL is about 17 nm, while in a crystalline phase, the length of the molecule is 5.2 nm (Scheme 1, left).[35] In solution, the thickness of the phospholipid shell depends on two factors: the structure of the hydrophobic bilayer (the degree of interdigitation of hydrophobic tails and oleic acid) and the coiling or stretching of the PEG tail. Because the length of the fully extended C_{18} tail is theoretically 1.7 nm, a major factor determining the thickness and surface potential of the lipid shell is probably the packing of the PEG tails. Different surface potential could affect the counterion cloud.

C.3. BMV Protein Self-Assembly around the HOOC-PEG-PL Coated NPs. While the HOOC-PEG-PL coated NPs are stable in pure water, an ionic strength of ∼1 M results in aggregation of nanoparticles. Therefore, a modification of the BMV capsid reassembling procedure with a buffer of lower ionic strength than in previously developed procedures is required (see details in the Experimental Part and Supporting Information).[25] Figure 4 shows the TEM images of VLPs formed by self-assembling of BMV proteins around 20.1, 10.6, and 8.5 nm spherical NPs.

The 10.6 and the 8.5 nm diameters are smaller than that of the inner cavity (∼18 nm) of the native capsid, while the 20.1 nm diameter exceeds it. While virion particles with T-numbers lower than the native $T = 3$ can be obtained by nanoparticle-templated assembly,[36,37] particles of a larger T number have not, mainly because of the difficulty in obtaining a homogeneous ensemble of spherical Au nanoparticle larger than 12−15 nm. In comparison, the iron oxide NPs used in this work are remarkably spherical, even at a diameter of 20 nm. These particles could lead to templated virus assembly beyond the native $T = 3$. Well-defined, spherical VLPs with a mean diameter of 41.3 nm and a standard deviation of 2.2% were obtained for 20.1 nm iron oxide cores. This observation explains the need for a larger number of capsid proteins (540) per NP.

The efficiency of encapsulation of the 20.1 nm cores was evaluated from TEM micrographs as the ratio of well-defined single VLPs and the total number of NPs and determined to
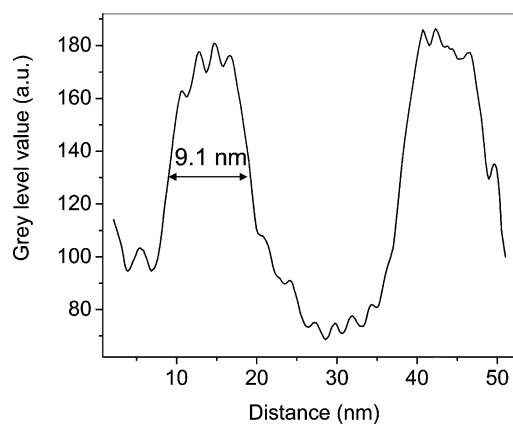

Figure 5. Average cross section through VLPs having a 20.1 nm diameter NP core. The shaded areas represent zones of lesser stain permeation associated with the hydrophobic domains of the protein shell and the lipid coat, together.

be 35 ± 5%. This efficiency is similar to the one found for 18 nm Au particles in ref 38.

It is noteworthy that, in the case of the 20.1 nm diameter NPs, the particle size distribution measured by TEM is slightly broader (4.1% standard deviation) than for the VLPs (2.2% standard deviation) templated over these functionalized NPs, revealing that the virus capsid self-assembling generates uniform VLPs.

The VLP shell thickness (lipid plus protein) can be estimated from an analysis of the TEM images. Figure 5 shows a cross section through the gray level values corresponding to an average of ten VLPs. The shell thickness is 9.1 ± 0.3 nm.

Considering that HOOC-PEG-PL lipid layer is about 4.0 ± 0.5 nm, and assuming that there is no significant interpenetration of protein and lipid, the BMV protein shell thickness should be ∼5.0 ± 0.5 nm. Taking into account the errors expected from negative staining fluctuations, the estimate comes reasonably close to the expected shell thickness for the native BMV (∼6 nm).[39] These results allow us to exclude the possibility of protein multilayers.
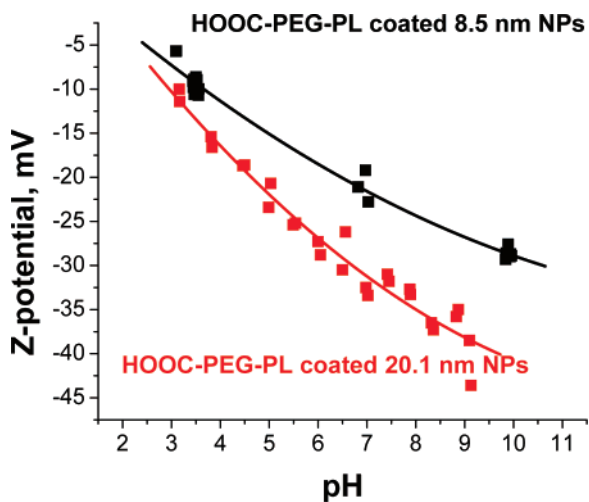
Figure 6. Zeta-potential as a function of pH for the 20.1 and 8.5 nm NPs functionalized with HOOC-PEG-PL.
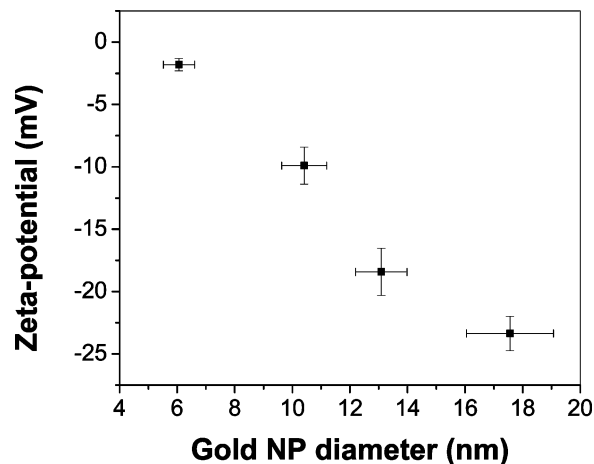

Figure 7. Zeta potential of functionalized gold nanoparticles at pH 7.0. The particles are coated with a covalently bound thiol (HOOC-PEG-SH) layer.[38]

Interestingly, smaller particles of 10.6 and 8.5 nm in diameter had a much lower efficiency of encapsulation (∼5%, and 3% respectively) than the 20.1 nm NPs. This contrasts with the case of gold cores of similar sizes, which had encapsulation efficiencies of ∼50%.[38] Moreover, magnetic VLPs encapsulating cores in the range 8−11 nm yielded irregular aggregates and a large fraction of empty capsids (Figure S5, Supporting Information), at the same and lower capsid protein per the NP ratio and at two ionic strengths (Table S1, Supporting Information). We observed that the smaller the particles, the higher the observed degree of VLP fusion, which is probably indicative of an unstable or incomplete capsid. Variations in the thickness of the protein layer with the core size were also observed, Figure 3. The question is whether these deviations from the Au core VLP characteristics and the core-size dependence of the assembly products have some common origin such as the surface charge.

To test the surface charge hypothesis, zeta-potential measurements were taken for the 20.1 and 8.5 nm magnetic NPs coated with HOOC-PEG-PL (Figure 6). At pH 7, the zeta-potentials of 20.1 and 8.5 nm core magnetic NPs are −32.8 and −22.8 mV, respectively. Because the zeta-potential measured for the lipid-coated magnetic NPs is greater or equal than that of the comparable Au NPs (Figure 7), the surface charge of PEG thiol-protected Au particles should be at least comparable with the phospholipid-protected NPs. The difference in encapsulation efficiency is then more likely to be related to the packing of the lipid coat, which depends on the NP size rather than on the total surface charge.

For $T = 3$ viruses, the net RNA charge (∼4000) is roughly twice the net capsid protein charge (∼1800). It would be interesting then to know how the nanoparticle surface charge compares with the native RNA.

To quantify the amount of the HOOC-PEG-PL molecules on the surface of NPs, we used ATR-FTIR. The intensity of the IR peak at 1740 cm^{-1} ascribed to C=O stretching vibrations was used to calibrate the HOOC-PEG-PL con-

centrations in aqueous solutions (see Supporting Information). At the same 1740 cm^{-1} peak intensity we found that the ligand density on the surface of the NPs (see Experimental Part) changed with the NP size (Table 1); ligand density increases roughly 2-fold between 8.5 and 20.1 nm diameter NPs, consistent with size-dependent packing.

Two models for the how packing density varies with the NP diameter were analyzed. In the first, we assumed that the HOOC-PEG-PL molecules are evenly distributed on the NP surface and in the shell (Scheme 1, right). As discussed above, in the solid state, the length of HOOC-PEG-PL is about 5.2 nm (Scheme 1, left). However in pure water, the PEG tail should be in a coil conformation. We used a value of 9 nm (see previous section) to estimate the shell size in solution for 20.1 nm diameter NPs. Because HOOC-PEG-PL has two "feet" and a bulky PEG head, we assumed the shape of the lipid is triangular (Scheme 1, right), where b is the length of the ligand (9 nm) and a is the width of the ligand as affected by the size of the PEG coil in water.
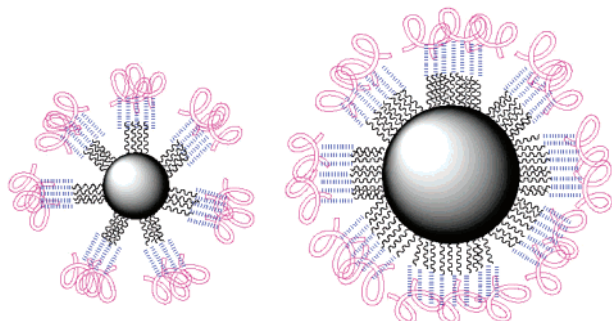
This model predicts an increase in the density with a decrease in the particle radius. Experimentally, we observed the opposite trend: ligand density increases with particle diameter. Since the main assumption of this model was that lipids are evenly distributed across the surface, we deduce that this is not the case.

The second model assumes an even distribution of surfactants on the NP surface but uneven location of terminal groups. The attachment of PEG lipids to the NPs occurs through the formation of a hydrophobic bilayer with the oleic acid, which acts as an initial stabilizing surfactant for NPs. It is well-established that on flat surfaces the surfactant hydrophobic tails tend to align parallel to each other in order to enhance hydrophobic interactions and minimize the free energy. Moreover, Luedtke and Landman used molecular dynamics simulations to show that on curved surfaces passivating molecules organize into preferentially oriented molecular bundles with the molecules aligned approximately parallel to each other (Scheme 2).[40] Scheme 2 suggests that the smaller NPs will have lower average density of these bundles at the NP exterior. The denser the brush, the more

Table 1. HOOC-PEG-PL Distribution on the NP Surface Derived from FTIR

NP size, nm	surface ligand density, number/nm^2	surface area per ligand, nm^2	shell size, nm (from DLS)	charge density,[a] COOH number/nm^2
20.1	3.50	0.285	9	1.67
10.6	2.52	0.397	14	0.47
8.5	1.85	0.539	11	0.35

[a] Charge density was calculated as a number of COOH groups per nm^2 assuming the stretching of HOOC-PEG-PL shell estimated from DLS measurements.

Scheme 2. Schematic Representation of Bundling of the Oleic Acid Tails and the HOOC-PEG-PL Molecules on the NP Surface Depending on the Core Size, PEG Tails Shown as Pink Coils

Figure 8. (a) Magnetization curve of 20.1 nm iron oxide NPs obtained at room temperature. The solid line here and in Figure 9 only guides the eye. (b) ZFC and FC curves of 20.1 nm iron oxide NPs.

favorable the conditions for the formation of a double hydrophobic layer of the lipid hydrophobic tails with the oleic acid tails, so this arrangement should remain after functionalization with PEGylated phospholipids.

The second model may explain the different behavior of gold and semiconductor nanoparticles stabilized with a carboxy-PEG thiol (HOOC-PEG-SH) ligand.[25,26] Even with much smaller nanoparticles (∼4−6 nm in diameter) the templating of BMV capsids was more regular than with the 8.5 nm iron oxide NPs coated with HOOC-PEG-PL. This could be explained by the fact that HOOC-PEG-SH ligands are much shorter than HOOC-PEG-PL (the extended length of HOOC-PEG-SH is only ∼2.7 nm,[25]), so curvature and bundling effects are less likely to influence their surface density.

We do not have at this point a firm explanation for this dependence, but if the NP preparation conditions yield same surface properties, the average curvature and faceting effects for particles of different sizes should be main candidates for an explanation of the radius-dependent lipid packing.

Carboxylate surface densities in Table 1 provide us with an estimate of the total surface charge. Thus, assuming that all ionizable groups are charged, 8.5 nm NPs should carry ∼400 charges, while 20.1 nm particles should have ∼4500 charges on their surface. For both kinds of NPs, the amount of charges is insufficient to completely neutralize the protein charge of a capsid. This is not a requirement for smaller capsids but may become one for capsids with T numbers larger than the native $T = 3$.

C.4. Magnetic Behavior of VLPs. Magnetic behavior of the NP cores was characterized using SQUID magnetometry. Figure 8a shows the magnetization curve of 20.1 nm NPs at room temperature. The lack of hysteresis at room temperature
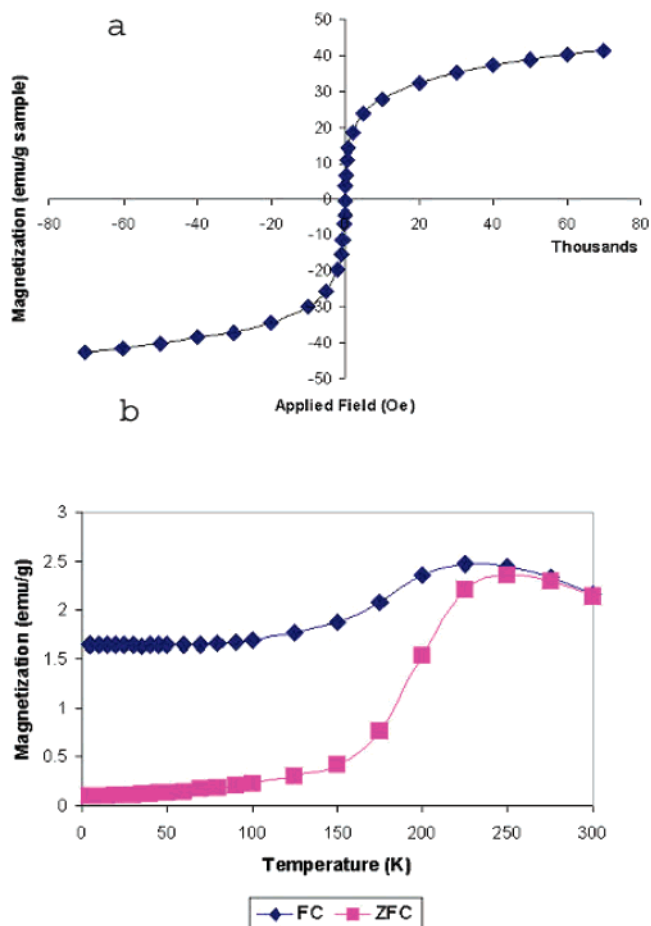
and the "S" shape of the curve are typical of superparamagnetic systems above the blocking temperature. Figure 8b presents field cooling (FC) and zero field cooling (ZFC) curves. The onset of hysteretic behavior, a proxy for estimating the blocking temperature, was observed at approximately 250 K.[21]

Confirmation of the magnetic character of magnetic VLPs based on iron oxide NPs was obtained from MFM measurements. The magnetic signal for the NP cores and magnetic VLPs was monitored by using the property of phase modulation by the magnetic coupling between the tip and the sample. This is done by measuring the phase lag ($\Delta\Phi$) between the piezo drive and the actual phase of oscillation for the cantilever which is described as having a quality factor Q and spring constant. The relationship between the mea-
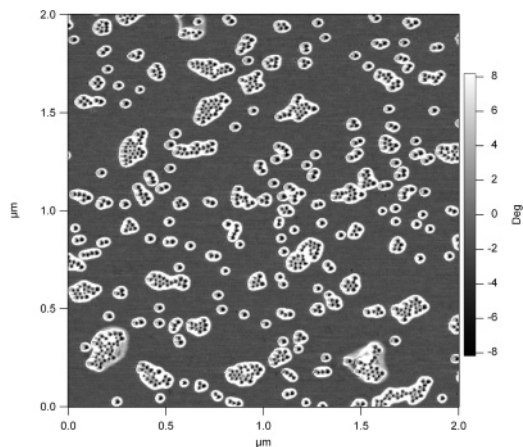
Figure 9. Phase image obtained by noncontact AFM showing two-dimensional islands and individual 20.1 nm diameter NPs on a mica substrate imaged in air.

sured signal and the force derivative can be described as follows:[41]

$$\Delta\Phi \sim \frac{Q}{k}\frac{\delta F}{\delta z}$$

Therefore, phase mapping with MFM can be used to provide quantitative information on the local magnetic field. For example, a comparison of the probability distribution of the phase shift with the size distribution would provide insight in the nature of magnetic domains of individual particles and its relationship with the particle size.[42,43] However, in our case, although individual particles were clearly resolved by ac noncontact AFM imaging under low concentration conditions (Figure 9) and superparamagnetic behavior in magnetometry measurements was observed (Figures 8, 9), no measurable magnetic signal was observed
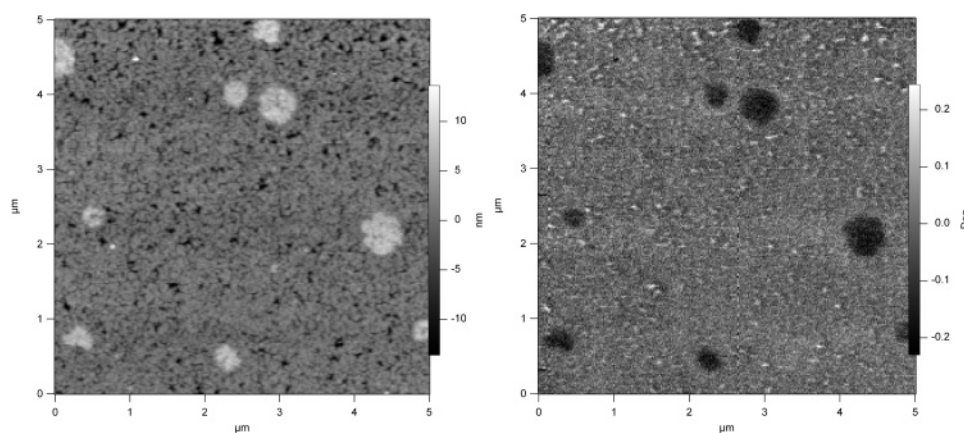

Figure 10. Topography (left) and magnetic signal (right) from a two-dimensional array of 20.1 nm diameter NPs. The magnetic trace was done at a lift height of 50 nm. Black regions correspond to an attraction and the white to a repulsive force.
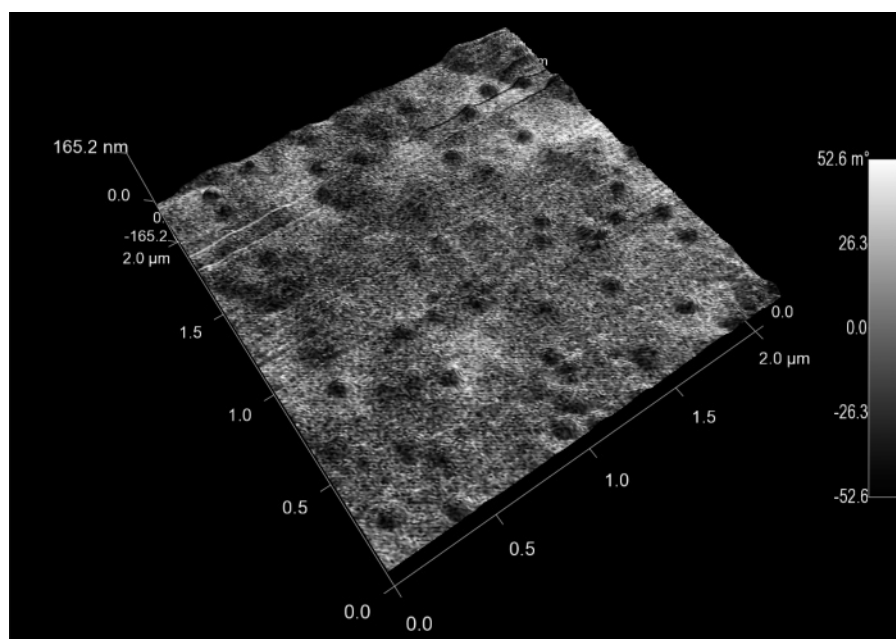

Figure 11. A spread of magnetic VLPs with 20.1 nm iron oxide cores imaged by MFM. The MFM phase contrast is overlaid over topography. Topography was encoded as three-dimensional appearance while the gray level value stands for phase change (magnetic signal). VLPs are therefore detectable by MFM although it is difficult to say with certainty whether they represent single particles or not because of the low spatial resolution of the MFM tip.

at a lift height of 50 nm from single particles. At closer tip–surface gaps, the imaging capability deteriorated rapidly probably due to the particles sticking to the tip during the scan.

At high particle concentrations, the NPs self-assembled into stable two-dimensional rafts when dried. From the topography image in Figure 10 two regions can clearly be distinguished, one corresponding to an incomplete monolayer (gray with dark spots) and the other to circular domains constituting a double layer (light gray). Both the first and second layers exhibit measurable magnetic coupling with the magnetic probe. Interestingly, the magnetic response of the double layer domains is different from the magnetic response of the first monolayer of particles underneath. Since the minimum size of the double layer domains that could be observed by MFM was ∼70 nm, we infer that these domains may contain at most 12 nanoparticles (Figure 11).

A similar phenomenon was observed with 12 nm Co nanoparticles by Puntes et al.[44] where it was determined that the particle density in an array would have a direct influence on the magnetic properties where the regions of lower density would result in stronger tip–sample interactions and the higher density areas would have weaker interactions due to the dipolar interactions of closely packed nanoparticles resulting in the magnetic moment remaining in-plane.[45]

In the case of superparamagnetic iron oxide NPs presented here, it appears that the thickness of the particle layers also affect the magnetic properties of the assemblies. The observed magnetic phase contrast between monolayer and double layer may be the result of different interactions at the interface between the two magnetic layers and between the first magnetic layer and the mica surface.

D. Conclusion. We have shown that it is possible to use a phospholipid micelle approach to obtain a magnetic nanoparticle template able to promote self-assembly of a protein cage and result in a VLP. VLP encapsulation efficiency was found to be strongly dependent on size, and the size effect is believed to be the result of lipid bundling when template curvature is comparable with the extended length of PEGylated phospholipid. VLPs larger in size than the $T = 3$ native viruses can be obtained using spherical iron oxide templates which shows the versatility of assembling viral protein containers that can accept larger loads than native viral particles. Such VLPs have superparamagnetic properties and may represent a promising route toward enhanced MRI mapping.

Supporting Information Available: Protocol of BMV assembling, table of experimental parameters used for VLP formation, and figures showing calibration of NP concentrations, TEM images or iron oxide NPs, coated NPs, and VLPs assembled with NP and proteins. This material is available free of charge via the Internet at http://pubs.acs.org.

References

(1) Bulte, J. W.; Kraitchman, D. L. *NMR Biomed.* **2004**, *17*, 484−499.
(2) Mulder, W. J. M.; Strijkers, G. J.; van Tilborg, G. A. F.; Griffioen, A. W.; Nicolay, K. *NMR Biomed.* **2006**, *19* (1), 142−164.
(3) Chemla, Y. R.; Crossman, H. L.; Poon, Y.; McDermott, R.; R;, S.; Alper, M. D.; Clarke, J. *Proc. Natl. Acad. Sci. U.S.A.* **2000**, *97* (26), 14268−14272.
(4) Pamme, N.; Wilhelm, C. *Lab Chip* **2006**, *6* (8), 974−980.
(5) Chatterjee, J.; Haik, Y.; Chen, C. J. *J. Magn. Magn. Mater.* **2001**, *225* (1−2), 21−29.
(6) Flenniken, M. L.; Willits, D. A.; Harmsen, A. L.; Liepold, L. O.; Harmsen, A. G.; Young, M. J.; Douglas, T. *Chem. Biol.* **2006**, *13* (2), 161−170.
(7) Douglas, T.; Young, M. *Science* **2006**, *312* (5775), 873−875.
(8) Chatterji, A.; Ochoa, W.; Shamieh, L.; Salakian, S. P.; Wong, S. M.; Clinton, G.; Ghosh, P.; Lin, T.; Johnson, J. E. *Bioconjugate Chem.* **2004**, *15* (4), 807−813.
(9) Loo, L.; Guenther, R. H.; Basnayake, V. R.; Lommel, S. A.; Franzen, S. *J. Am. Chem. Soc.* **2006**, *128* (14), 4502−4503.
(10) Dragnea, B.; Chen, C.; Kwak, E. S.; Stein, B.; Kao, C. C. *J. Am. Chem. Soc.* **2003**, *125* (21), 6374−6375.
(11) Pouliquen, D.; Perdrisot, R.; Ermias, A.; Akoka, S.; Jallet, P.; Le Jeune, J. J., 7(6), 619−27. *Magn. Reson. Imaging* **1989**, *7* (6), 619−627.
(12) Shapiro, E. M.; Skrtic, S.; Sharer, K.; Hill, J. M.; Dunbar, C. E.; Koretsky, A. P. *Proc. Natl. Acad. Sci. U.S.A.* **2004**, *101* (30), 10901−10906.
(13) Schneider, B. *Prog. Bot.* **2004**, *65*, 301−322.
(14) Lambert, J.; Lampen, P.; Bohlen, A.; Hergenroeder, R. *Anal. Bioanal. Chem.* **2006**, *384* (1), 231−236.
(15) Giddings, G.; Allison, G.; Brooks, D.; Carter, A. *Nat. Biotechnol.* **2000**, *18* (11), 1151−1155.
(16) Lucas, R. W.; Larson, S. B.; McPherson, A. *J. Mol. Biol.* **2002**, *317* (1), 95−108.
(17) Kaper, J. M. *The Chemical Basis of Virus Structure, Dissociation and Reassembly*; North-Holland: Amsterdam., 1975; pp 333−352.
(18) Bancroft, J. B.; Bracker, C. E.; Wagner, G. W. *Virology* **1969**, *38*, 324−335.
(19) Douglas, T.; Young, M. *Nature* **1998**, *393* (6681), 152−155.
(20) Allen, M.; Willits, D.; Mosolf, J.; Young, M.; Douglas, T. *Adv. Mater* **2002**, *14* (21), 1562−1565.
(21) Talapin, D. V.; Shevchenko, E. V.; Weller, H., Synthesis and Characterization of Magnetic Nanoparticles. In *Nanoparticles*; Schmid, G., Ed.; Wiley-VCH: Weinheim, 2004; pp 199−230.
(22) Park, J.; An, K.; Hwang, Y.; Park, J.-G.; Noh, H.-J.; Kim, J.-Y.; Park, J.-H.; Hwang, N.-M.; Hyeon, T. *Nat. Mater.* **2004**, *3* (12), 891−895.
(23) Hyeon, T.; Lee, S. S.; Park, J.; Chung, Y.; Na, H. B. *J. Am. Chem. Soc.* **2001**, *123*, 12798−12801.
(24) Dragnea, B.; Chen, C.; Kwak, E.-S.; Stein, B.; Kao, C. C. *J. Am. Chem. Soc.* **2003**, *125* (21), 6374−6375.
(25) Chen, C.; Daniel, M.-C.; Quinkert, Z. T.; De, M.; Stein, B.; Bowman, V. D.; Chipman, P. R.; Rotello, V. M.; Kao, C. C.; Dragnea, B. *Nano Lett.* **2006**, *6* (4), 611−615.
(26) Dixit, S. K.; Goicochea, N. L.; Daniel, M.-C.; Murali, A.; Bronstein, L.; De, M.; Stein, B.; Rotello, V. M.; Kao, C. C.; Dragnea, B. *Nano Lett.* **2006**, *6* (9), 1993−1999.
(27) Gopinath, K.; Dragnea, B.; Kao, C. *J. Virol.* **2005**, *79* (22), 14222−14234.
(28) Bronstein, L. M.; Huang, X.; Retrum, J.; Schmucker, A.; Pink, M.; Stein, B. D.; Dragnea, B. *Chem. Mater.*, **2007**, *19*, 3624−3632.
(29) Dubertret, B.; Skourides, P.; Norris, D. J.; Noireaux, V.; Brivanlou, A. H.; Libchaber, A. *Science* **2002**, *298* (5599), 1759−1762.
(30) Dixit, S. K.; Goicochea, N. L.; Daniel, M. C. *Nano Lett.* **2006**, *6* (9), 1993−1999.
(31) Chen, C.; Daniel, M.-C.; Quinkert, Z. T.; De, M.; Stein, B.; Bowman, V. D.; Chipman, P. R.; Rotello, V. M.; Kao, C. C.; Dragnea, B. *Nano Lett.* **2006**, *6* (4), 611−615.
(32) Nitin, N.; LaConte, L. E. W.; Zurkiya, O.; Hu, X.; Bao, G. *J. Biol. Inorg. Chem.* **2004**, *9* (6), 706−712.
(33) Lim, Y. T.; Lee, K. Y.; Lee, K.; Chung, B. H. *Biochem. Biophys. Res. Commun.* **2006**, *344* (3), 926−930.
(34) Xie, J.; Peng, S.; Brower, N.; Pourmand, N.; Wang, S. X.; Sun, S. *Pure Appl. Chem.* **2006**, *78* (5), 1003−1014.

(35) Zanchet, D.; Micheel, C. M.; Parak, W. J.; Gerion, D.; Williams, S. C.; Alivisatos, A. P. *J. Phys. Chem. B* **2002**, *106*, 11758−11763.

(36) Krol, M. A.; Olson, N. H.; Tate, J.; Johnson, J. E.; Baker, T. S.; Ahlquist, P. *Proc. Natl. Acad. Sci. U.S.A.* **1999**, *96* (24), 13650−13655.

(37) Lucas, R. W.; Kuznetsov, Y. G.; Larson, S. B.; McPherson, A. *Virology* **2001**, *286* (2), 290−303.

(38) Sun, J.; DuFort, C.; Daniel, M.-C.; Murali, A.; Chen, C.; Gopinath, K.; Stein, B.; De, M.; Rotello, V. M.; Holzenburg, A.; Kao, C. C.; Dragnea, B. *Proc. Natl. Acad. Sci. U.S.A.* **2006**, *104*, 1354.

(39) Lucas, R. W.; S. B. Larson; McPherson, A. *J. Mol. Biol.* **2002**, *317* (1), 95−108.

(40) Luedtke, W. D.; Landman, U. *J. Phys. Chem. B* **1998**, *102* (34), 6566−6572.

(41) Hartmann, U. *Annu. Rev. Mater. Sci.* **1999**, *29*, 53−87.

(42) Rasa, M.; Kuipers, B. W. M.; Philipse, A. P. *J. Colloid Interface Sci.* **2002**, *250* (2), 303−315.

(43) Proksch, R. B.; Schaffer, T. E.; Moskowitz, B. M.; Dahlberg, E. D.; Bazylinski, D. A.; Frankel, R. B. *Appl. Phys. Lett.* **1995**, *66* (19), 2582−2584.

(44) Puntes, V. F.; Gorostiza, P.; Aruguete, D. M.; Bastus, N. G.; Alivisatos, A. P. *Nat. Mater.* **2004**, *3* (4), 263−268.

(45) Georgescu, M.; Klokkenburg, M.; Erne, B. H.; Liljeroth, P.; Vanmaekelbergh, D.; van Emmichoven, P. A. Z. *Phys. Rev. B* **2006**, *73* (18).

NL071083L